EMAS Engineering Modelling, Analysis & Simulation THE NAFEMS JOURNAL

NAFEMS

Vol. 2, Issue 1, 2025

Simulation and physical validation of metal triply periodic minimal surfaces-based scaffolds for bioengineering applications

M. Khalil[a], M. Burton[a], S. Hickinbotham[b], P. P. Conway[a], C. Torres-Sanchez[a,1]

[a]Multifunctional Materials Manufacturing Lab, Wolfson School, Loughborough University, Leics LE11 3TU, UK

[b]Department of Electronics Engineering, University of York, York YO10 5DD, UK

Abstract

Metallic scaffolds are used as implants to help heal bones. Sheet-based Triply Periodic Minimal Surfaces (TPMS) are of interest due to their high surface-to-volume ratio (S/V) and customisable stiffness. They can be realised using Additive Manufacturing (AM). Other studies investigate porosity and pore size of scaffolds, but they frequently overlook S/V, which is critical for cellular response. Additionally, the limitation of AM (esp. Selective Laser Melting (SLM)) resides in the discrepancies between as-designed and as-built physical and mechanical properties of those structures, and this also needs addressing. This work investigates three types of pure Titanium TPMS scaffolds, with an emphasis on as-designed vs as-built discrepancies and the significance of S/V. As-designed scaffolds reported 70-75% porosity and 25-35 cm^{-1} S/V, and stiffness was measured using finite element analysis (FEA) obtaining 6.7-9.3 GPa. The as-built scaffolds had 59-70% porosity and 33-42 cm^{-1} S/V. Laboratory compression testing revealed an effective Young's modulus of 5-9 GPa, comparable to bone tissue. Image-based simulation methods were employed on the as-built samples which reported the stiffness range of 8.3-15 GPa, overestimating it by 54%. It is hypothesised that these discrepancies stem from the secondary roughness on the surfaces, cracks and entrapped voids created during the SLM process, causing reduction in porosity, yet not contributing to structure's strength. The cyber-physical validation methods presented in this work are a good way to quantify these discrepancies, allowing feedback to the design stages for more predictable as-built structures.

Keywords

Triply periodic minimal surface, Selective Laser Melting, Surface area per unit volume, Finite Element Analysis, Meshless method, Validation.

1 Introduction

Lattice structures are a type of porous material different from foams and honeycombs. Their cell topology, scale and properties are different from each other [1]. Strut-based and triply periodic minimal surface (TPMS) lattice structures are becoming popular in biomedical applications due to their multifunctional capability to match the mechanical strength and other physical properties of bone structures [2], [3]. In addition, the porous structure, with suitable pore size and porosity, can provide enough space for cellular proliferation. The TPMS structures are classified into two types according to the topological-property relationship: sheet solid and network solid [4]. Compared to a network solid, sheet solids possess superior mechanical properties as well as higher S/V and permeability values and lower wall shear stresses, which are favourable for biomechanical environment [5], [6].

[1]Corresponding author.
E-mail address: c.torres@lboro.ac.uk (C. Torres-Sanchez)
https://doi.org/10.59972/fn8161af

Literature suggests that the optimum bone tissue engineering scaffold has macro-pores of size larger than 300 μm and porosity larger than 50% [2]. Sheet-based gyroids [3], [7]–[11], diamond and primitive [8] structures are most frequently reported for bone applications. They used porosity and pore size as the key design parameters for their work. While discrepancies have been reported between as-designed and as-built structures but only a few of them [3], [8] have included the S/V values in the studies as well.

One of the most common technologies to manufacture these structures is Selective Laser Melting (SLM) which has many advantages compared to conventional manufacturing processes, including no geometric restrictions, near-net shape and lower production lead time [12]. However, SLM has its limitations to wall inclination of the structure when printing. The layer-by-layer printing process causes staircase effect which contributes to poor surface roughness on the overhangs [13]. The inclination angle of walls continuously varies in TPMS structures, which means past layers support subsequent layers, enhancing manufacturability of these structures by SLM [14].

To understand the structural behaviour of the scaffolds under varying loads, simulators based on Finite Element Analysis (FEA) provide an affordable substitute for expensive experimental testing. They are an effective tool when simulation parameters are defined properly. However, lattice structures are difficult to simulate because of their complex geometry, which requires a lot of processing power and sophisticated meshing [15]. FEA of a full lattice structure was performed in few studies [7] while others preferred homogenization methods, which substitutes the single unit cell with an equivalent built elastic material model [16]. Mesh convergence and lattice tessellation studies are used to determine the suitable mesh/model size to obtain estimated mechanical properties of lattices at lower simulation costs [10], [17]. Most studies report overpredictions of mechanical properties by numerical method approach despite a reduction in the as-built porosity of the lattices [7], [10], [11]. These differences are caused by the geometric deviation due to SLM manufacturing limitations, internal defects and secondary surface roughness [7].

For more accurate simulations compared to idealized CAD-based methods, image-based simulation methods are used. These rely on digital representations of real geometries from image data. The most common method of scanning the scaffolds is via computer tomography (CT). However, the CT scan resolution is a major hurdle to capture the full detail of all material imperfection, compromising the integrity of the structural model [18]. Various image processing approaches have been tested, such as underestimating the material properties, adjusting image threshold levels or combinations of filtering and morphological operations to get closest to the actual microstructure [19], [20]. Though the results were promising, they are limited to the fact that only a very small fraction of as-built sample was used for FEA simulation due to computer hardware limitation. Mahmoud et al. [21] used the model of a single unit cell of the structure to run image based simulation. However, the mesh quality and element size, as well as the model size highly affect the simulation cost and output. An alternative approach is offered by meshless methods which can be applied to the original, native, and non-simplified geometric models avoiding FE mesh problems due to geometric complexity and size [28].

The aim of this study is to evaluate the manufacturability of three commonly used types of sheet-based TPMS structures (i.e., gyroid, primitive and diamond) designed to have connected porosities 70-75% and S/V between 25-35 cm^{-1} which mimic bone characteristics. This is a novelty over other reported studies. 3D metrological characterization by X-ray μ-CT imaging was performed and designed/built structures were compared. In addition, image-based simulations were performed on as-built structures using a meshless technique to determine their stiffness and compared with design simulation (by FEA) and lab test results. The results of this validation techniques can be helpful to understand the design/built variations and may be used to provide input to the design phases and produce more consistent as-built structures.

2 Materials and Methods

2.1 Scaffold Structure Design

The candidate TPMS structures were generated using MATLAB (revision R2021A) and Blender (version 2.93). The process of generating the structures was automated using a script written in Python 3.9. The MATLAB-driven processes generated a linear-spaced vector of points in 3D that are used to sample the continuous TPMS functions at a resolution of 100 points in each dimension. MATLAB's isosurface and isocaps functions were then used to mesh these points into 10 mm-side cubes. For each formulation, two "surface" type structures were generated in this way by offsetting the TPMS mesh

coordinates in opposite directions and saved as STL files. These STL files were then imported into Blender, which was used to remesh and decimate the resulting STL files to ensure the meshes were watertight. A Boolean operation was then carried out to subtract one mesh from the other to create a physical, thick, manifestation of the TPMS surface. Finally, Blender was used to record the volume and surface area of the resulting structure, which was exported to a final STL file for manufacturing purposes.

Three TPMS formulations were evaluated: gyroid ("G"); primitive ("P") and diamond ("D"). Each of these was evaluated for wall thickness between 0.1 and 0.8 mm with step size 0.1, and number of cycles per 10 mm between 5 and 12 inclusive. A total of 192 structures were generated in this way.

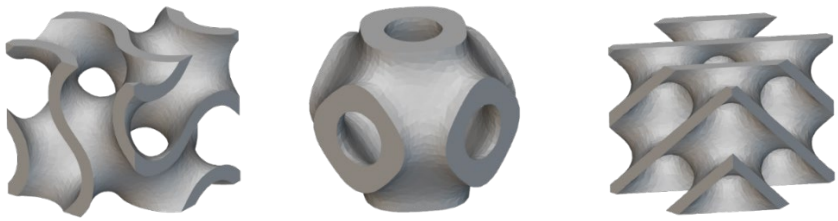

Gyroid Primitive Diamond

Figure 1. Examples of a unit cell of each type of scaffold included in this study.

From the three types evaluated, the variants that fulfilled the criteria (i.e. intended porosity range of 70-75% and 25-35 cm^{-1} surface area per unit volume) were shortlisted.

Table 1. Intended physical properties of as-designed scaffolds.

Structure	Scaffold ID	Unit cell size (μm)	Porosity (%)	S/V (cm^{-1})	Sheet thickness (μm)	Pore Size (μm)
Gyroid	G2.50	2500	73.9	25.2	254 ± 6	872 ± 88
	G2.22	2222	73.8	28.2	229 ± 5	779 ± 77
Primitive	P1.64	1667	70.9	28.2	254 ± 22	831 ± 311
	P1.43	1428	70.6	32.8	225 ± 18	720 ± 280
Diamond	D2.50	2500	74.9	30.9	205 ± 4	761 ± 99
	D2.22	2222	74.8	34.7	188 ± 2	681 ± 81

2.2 Static Analysis of Scaffolds

The FE analysis of the scaffolds was carried out in nTop (nTopology Inc. USA) software on a workstation with two 10 cores Intel Xeon E5-2660 v3 CPUs and 64GB memory. Linear static analysis was run to estimate the effective elastic modulus of the lattices. The STL models were meshed using quadratic tetrahedral elements in nTop. The resultant FE models were subjected to compressive displacement of 0.02 mm at the nodes of their top surfaces. These nodes were completely constrained and subjected to translate along z axis only. The movement of the nodes on bottom surfaces was fully restricted (Figure 2.a.). The elastic modulus was calculated using the following equation,

$$Effective\ elastic\ modulus, E = \frac{\frac{F}{A}}{\frac{\Delta L}{L}}, \quad (1)$$

where F is the total reaction force (N) at the bottom nodes, A is the cross-sectional area of the sample, L is the scaffold's original height (mm) and ΔL is the displacement applied (mm) at top nodes.

An elastic modulus of 76.7 GPa was assigned to FE elements in the model. This value was obtained from lab compression testing (as per ASTM E9-19 standard [22]) of Solid cylinders (grade 1 cp-Ti) printed by SLM on the same build plate of scaffolds with similar printing parameters (Section 2.3).

A meshless method was adopted for static analysis of digital models of as-built samples using Altair SimSolid 2023 (Altair Engineering Inc. USA) software. The sample's STL file (generated from CT data, see section 2.4) was imported in SimSolid and similar material properties were assigned to it as in the case of nTop simulations. The lattice model was compressed between top and bottom rigid plates, which were modeled in Magics v.22.03 (Materialise, Belgium) software before importing in SimSolid (Figure 2.b.). Immovable boundary condition was applied to the bottom plate while the top plate was

displaced 0.02 mm in the –z axis direction, and all other linear and rotational movements were restrained. The resultant reaction force on the bottom surface was used in Equation 1 to calculate the elastic modulus. To enhance the solution's accuracy, the solution parameters such as "adapt to features" and 'adapt to thin solids" were turned-on with a minimum of 6 solution iterations.

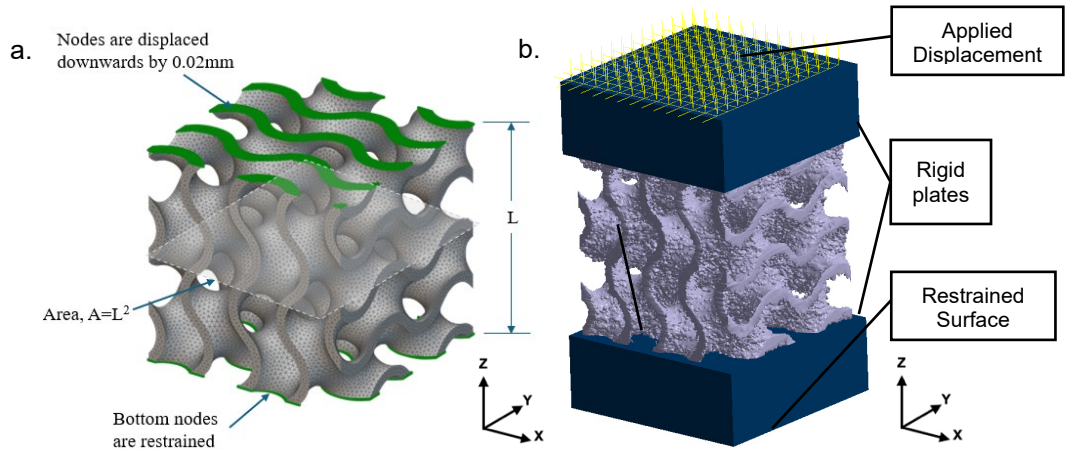

Figure 2. A depiction of boundary conditions applied to the scaffold (gyroid 2x2x2 cells), a. for FEA in nTop, b. As-built scaffold model compressed between rigid plates in SimSolid.

2.3 Scaffolds Manufacturing

The scaffolds were manufactured using a SLM AM process in a TruPrint 1000 LMF (Trumpf, Germany) machine. A 200W Nd:YAG solid-state laser with a 55 µm spot size was used in an argon environment (<100 ppm oxygen content). To produce a volumetric energy density of 30 J mm^{-3}, the laser scanning parameters employed were a laser beam power of 140 W at a speed of 1,414 mm s^{-1}, a hatch distance of 0.11 mm, and a layer thickness of 0.03 mm. A boundary offset of 0.05 mm and a 90° rotation between the layers were used in the zigzag scanning technique.

The scaffolds were printed using grade 1 cp-Ti powder. The spherical gas-atomized powder (AP&C, GE Additive, Canada) had a particle size distribution in the range as per testing method ASTM B822-17; 45-15 µm of D10 (19 µm), D50 (34 µm), and D90 (47 µm) with apparent density of 2.63 g cm^{-3}, as per ASTM B212-17. The chemical composition was determined as per ASTM E1941-10, E1409-13, E1447-09, E2371-13 standards [23]–[26] (Table 2).

Table 2. Chemical composition of Cp-Ti power.

Element	C	O	N	H	Fe	Other	Ti
Weight %	0.01	0.10	0.01	0.002	0.03	<0.2	Balance

Two sets of scaffolds were printed. First set, for morphological characterization, cubes of 1 cm^3 size. Second set, for compression testing, cubes of 1 cm^3 (in triplicate) including a solid layer of 2 mm on top/bottom as per BS ISO 13314 to mimic the simulation compression study. In addition, two solid samples of cylindrical shape with 10 mm diameter and 16 mm height were also printed for determination of material's mechanical properties. An additional 1 mm solid thickness was provided under each sample as a margin for slicing them off the plates. All samples were sliced off from the build pate using high speed diamond saw (IsoMet High Speed Saw, Buehler, Germany) and cleaned in an ultrasonic bath using acetone for 1 hour.

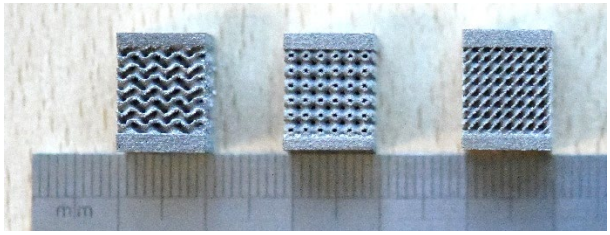

Figure 3. Compression test samples with top and bottom 2 mm solid thickness plates. Variants G2.22, P1.43 and D2.22 (from left to right).

2.4 Physical Characterization

To characterize the porosity (φ) of the as-built samples, a 2-step method was used. First, the dry porosity (ASTM F2450-18 standard) using the following two equations was measured,

$$vol\% = \frac{m_s}{m_d}, \tag{2}$$

$$\varphi\ (\%) = (1 - vol\%)x\ 100\ , \tag{3}$$

where m_s is mass of scaffold, m_d is the mass of fully dense structure obtained by multiplying the bulk volume and bulk density of the material (4.51 g/cm^3 for grade 1 cp-Ti).

Subsequently, acetone, a liquid with a low surface tension, was used as the immersion medium and the open porosity was determined using Archimedes' method.

The samples of size 10x10x10 mm^3 were scanned in Phoenix v|tome|x M (Waygate Technologies, Germany) micro computed tomography (µ-CT) system with 10.03 µm resolution at 180 kV and 50 µA using 0.5 mm copper filter. Images were reconstructed using a beam hardening correction value of 8 as a 3D volume in 16-bit data format. Contrast enhancement was applied to normalise the grey value range of each scan in VG Studio MAX v3.4 (Volume Graphics GmbH, Germany) by remapping the grey value for the background air in the image to 10,000 and then the fused titanium to 30,000. Data were then exported as a stack of .TIF images with voxel resolution of 0.01003 mm in XYZ for all samples.

The volumes were exported, segmented, and reconstructed in a 3D image analysis software ORS-Dragonfly (Comet Technologies Canada Inc.). The image stacks were filtered and then segmented using Otsu's thresholding method. Parameters such as porosity, surface area, deviation to as-designed geometry, wall thickness and pore sizes were measured. The as-designed STLs were rasterized to image stacks using a Python script in an open-source software, 3D Slicer [27]. These images were imported into Dragonfly to measure wall thickness and pore sizes of as-designed lattice geometry. The 'Sphere fitting method' [28] was used to measure the wall thickness and pore size of the scaffolds. Median and median absolute deviation (MAD) values were used for wall thickness and pore size, rather than mean and standard deviation due to a non-normal distribution of values [29].

2.5 Mechanical Characterization

A UTM (Instron 3369, UK) with a 50 kN (Instron 2530-445, UK) load cell was used for a single loading cycle of quasistatic compression testing of each sample (BS ISO 13314 standard). In order to minimise compliance errors, a constant strain rate of 0.01 mm/sec was applied, and the displacement of the top platen was recorded with an LVDT (Instron 2601-062, UK) with accuracy ± 6.25 µm. The preload was set to 3 N and all samples were compressed up to 30% of their gauge height. Parameters such as length, width, gauge height, total height and weight of test samples were measured prior to each test.

The raw data from the machine was used to plot stress-strain diagrams. Strain was calculated by diving the LVDT displacement by the specimen's gauge height. Stiffness was calculated from the linear slope displayed in the elastic region of region of the stress-strain curves. Yield strength was calculated using the 0.2% strain offset method.

3 Results and Discussion

3.1 Mesh Convergence Study

A comprehensive mesh convergence study was run in nTop on as-designed models of G2.22, P1.43 and D2.22 scaffolds; one variant from each structure type. The mesh element's edge length was varied in the range of 0.04-0.22 mm for 1x1x1 to 7x7x7 lattice models creating around 900 to 12,000,000 elements in total (900-170,000 elements per unit cell). The resultant modulus values were plotted against the number of finite elements per unit cells in Figure 4. However, the full range of element sizes could not be applied to larger models due to memory limitation of PC workstation used in this study.

We found that the modulus values converge at around 20,000 elements per unit cell in primitive structure, and around 60,000 elements in gyroid and diamond per unit cell. This is in close agreement with the work of Maskery et al. [30] who found 50,000 elements to be sufficient to reduce the FE discretization errors to insignificant levels. However, it needs to be pointed out that they evaluated mesh convergence of network based TPMS structures using voxel mesh on a different FEA solver.

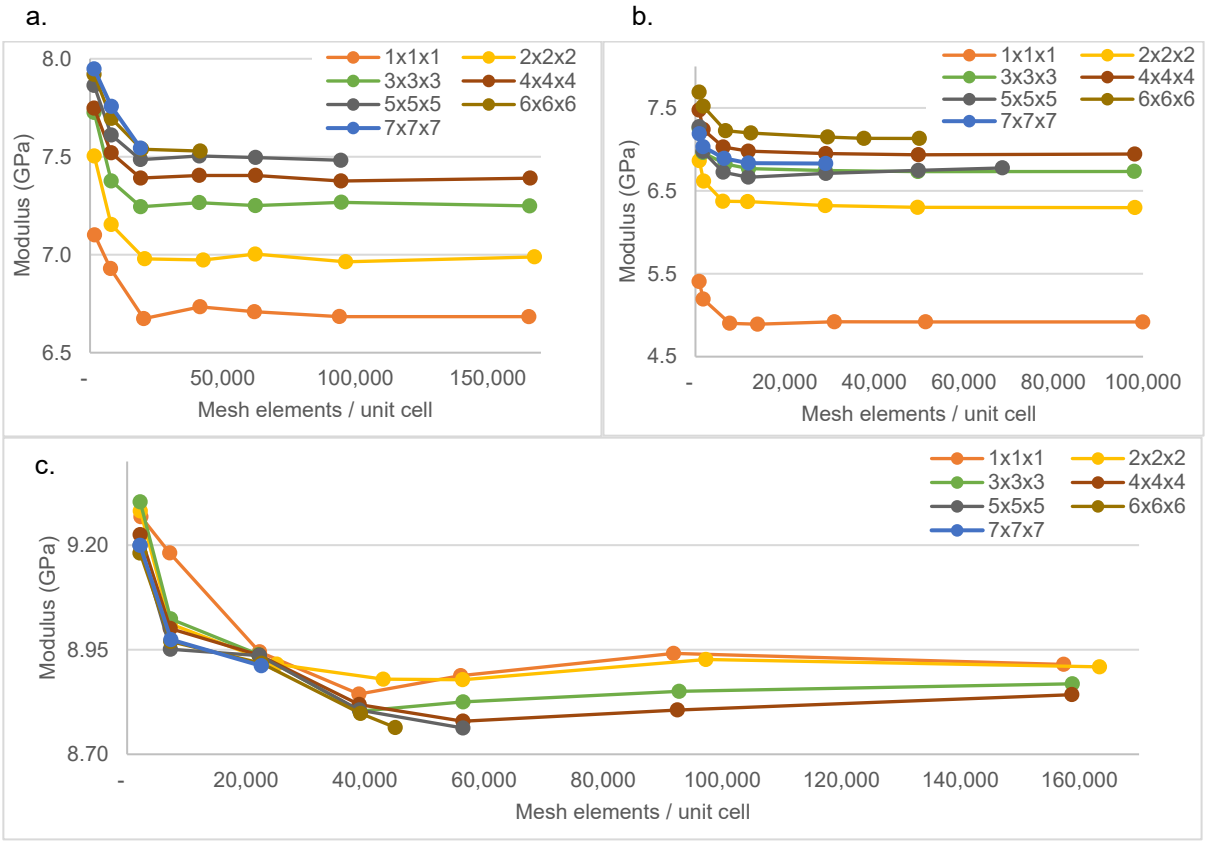

Figure 4. Finite element mesh convergence study for lattice structures comprising 1 × 1 × 1 to 7 × 7 × 7 cells. a. G2.22, b. P1.43, c. D2.22.

3.2 Scaffold Cell Tessellation Study

Since the lattices comprise unit cells repeated in space along three axes, it is important to know how many cells are sufficient for a FEA study without compromising the solution's accuracy and keeping a low simulation cost. Figure 5 shows the three lattice structures with a highlighted single unit cell.

The scaffold cell tessellation study was conducted by FE and meshless methods on the same three as-designed variants for which mesh convergence study was done in Section 3.1.

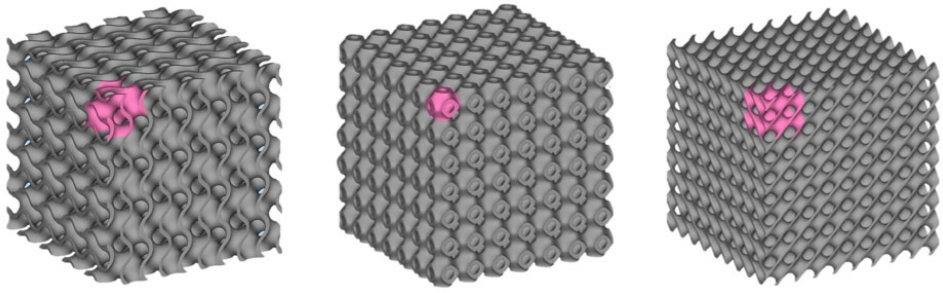

Figure 5. 1 cm^3 scaffold variants, G2.22, P1.43 and D2.22 (left to right), having 4.5, 7 and 4.5 unit cells respectively. Unit cells are highlighted in each scaffold.

3.2.1 FE Method

The converged moduli from section 3.1 were plotted against cell order in Figure 6. The moduli plateaued for larger than 4x4x4 cell configurations for gyroid and primitive structures. This is similar to the findings of Maskery et al. [30] and Simsek et al. [17] who evaluated network-based and sheet-based TPMS structures, respectively. However, we found that the diamond structures appeared to be the least affected with lattice tessellation with similar moduli for all lattice orders.

3.2.2 Meshless Method

The lattice cell tessellation study of as-designed models was performed in SimSolid also to validate the use of a meshless method for this study. The moduli obtained both methods were compared (Figure 6). Results for primitive structures (Figure 6.b.) were found to be very similar except for lattice order 5 and 7. For gyroid (Figure 6.a.) and diamond (Figure 6.c.) structures, results matched until lattice order 5 with both curves displaying marked increase in the meshless results.

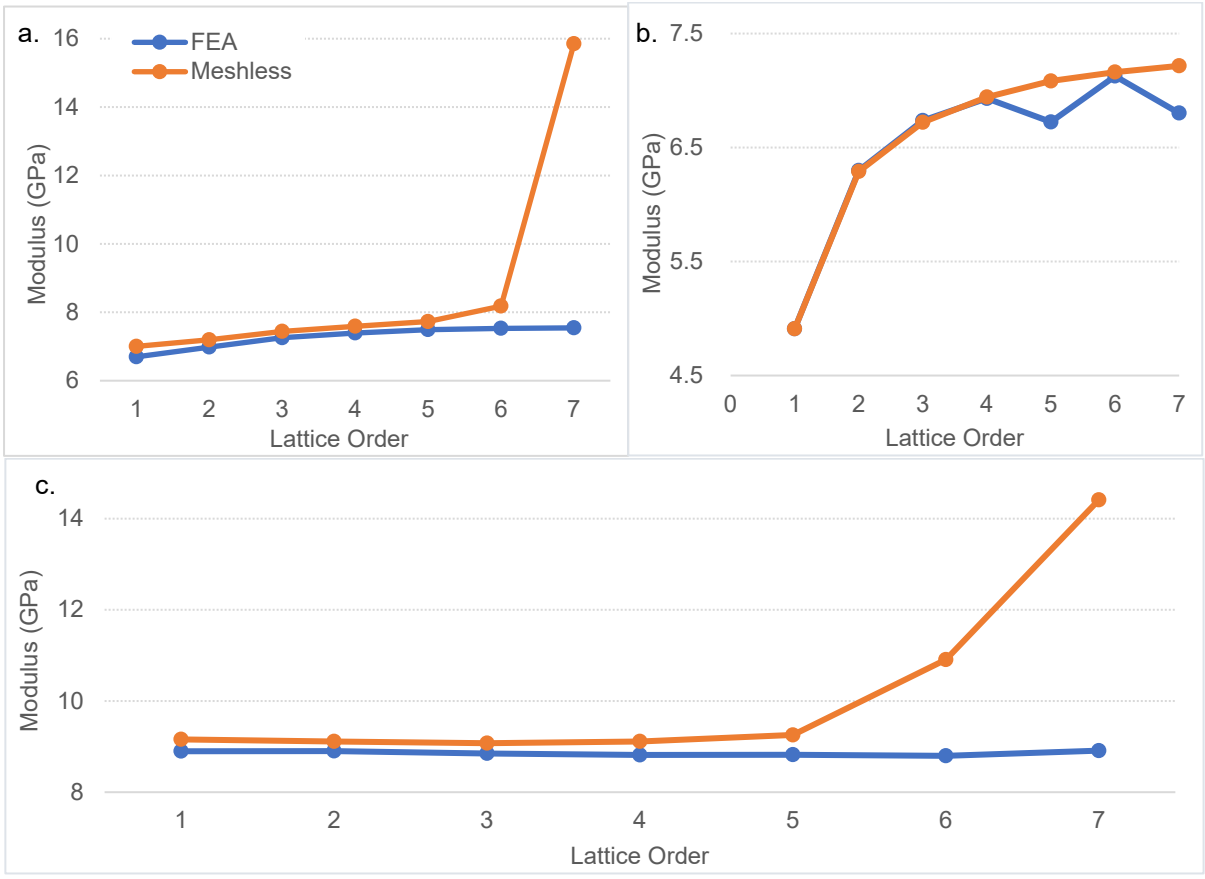

Figure 6. Lattice cell tessellation study of as-designed scaffold models by FEA and meshless methods. Effective elastic modulus plotted against increasing number of lattice unit cells. a. G2.22, b. P1.43, c. D2.22.

It is hypothesized to be due to the limitation of SimSolid to handle the size of the STL model files as larger models contain high number of mesh elements. To confirm this hypothesis, the lattice models of order 6 and 7 were split into parts equal to the unit cell size of the structure (Figure 7.d.). These parts were held together by rigid connections between them. The updated simulation results show (Figure 7.a. and b.) significant reduction in moduli. However, the meshless results of as-designed models were still around 4% higher than the average compared to the FEA results.

Moving forward, all following results in this study were obtained with 4^3 cells size for as-designed (FE method) as well as as-built models (meshless method). An FE mesh element size of 0.07mm was used for all scaffold structures.

3.3 Morphological Characteristics of Scaffolds

The micro-CT images of scaffolds show instances of closed porosity in the structures caused by the inherent nature of SLM process (arrows in Figure 8.a.) [31]. In addition, the surfaces were very rough and partly sintered metallic particles (secondary roughness [32]) were seen attached to the scaffold walls.

Figure 8.b. illustrates the deviation map of the built scaffold when compared to the as-designed model. Higher deviations were found on the overhangs on the bottom surfaces, contributing to a reduction in overall porosity.

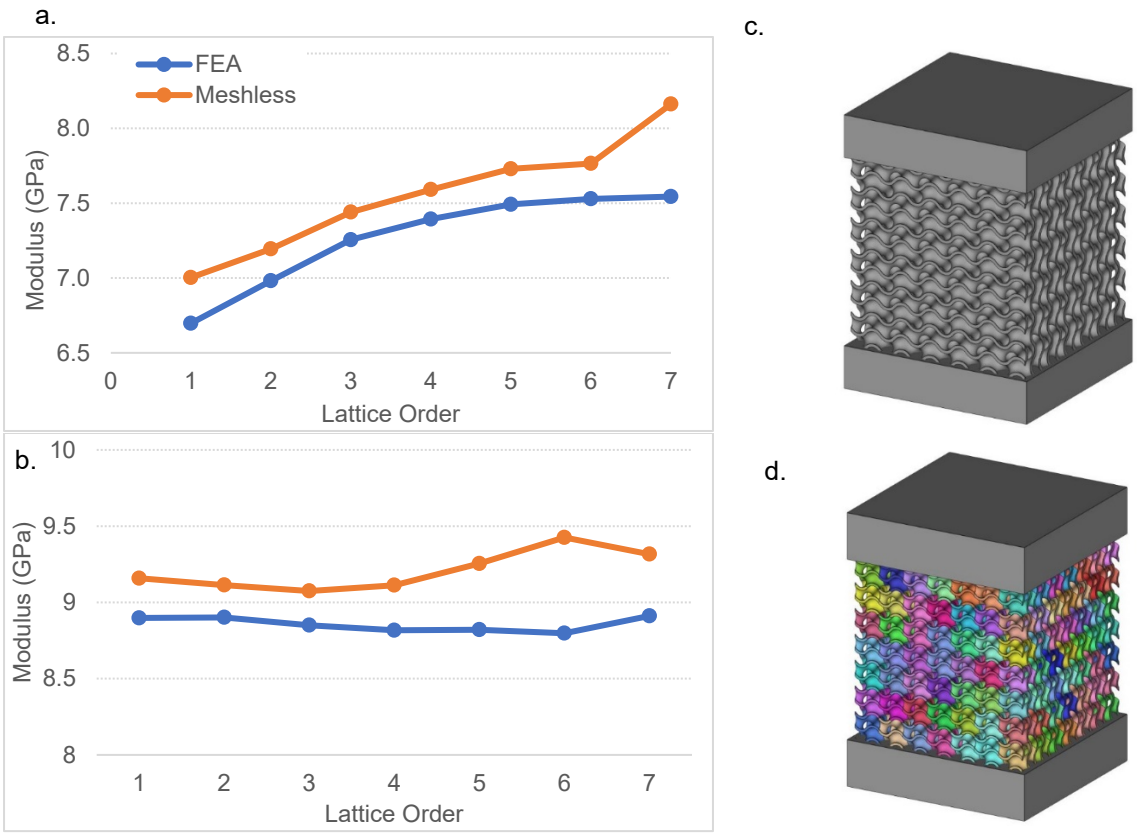

Figure 7. Revised lattice cell tessellation study based on model splitting into unit cells for a. G2.22 and b. D2.22 scaffolds. Unsplit (c.) and split (d.) models of G2.22 (7x7x7 cells).

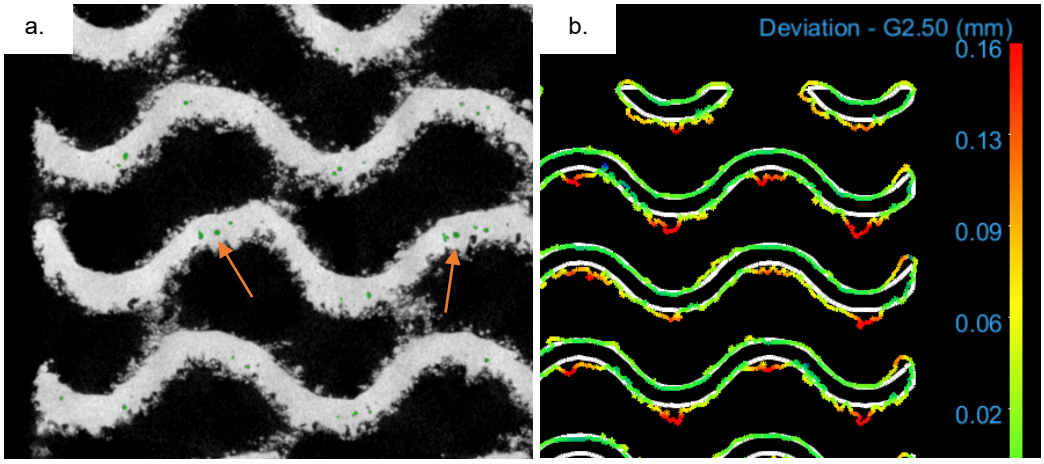

Figure 8.a. Slice of 3D tomographic image of G2.50, closed porosities in green and cp-Ti phase in grey colour, b. Geometrical deviation map created by overlaying as-built on the as-designed (in white) geometry. Overhangs can be spotted in red colour.

Both variants from each structure i.e. gyroid, primitive and diamond were intended to have the same open porosity. Our results show a reduction in as-built porosity for all samples when measured by dry mass, acetone and μ-CT methods. Scaffolds designs with smaller unit cell size (G2.22, P1.43 and D2.22) deviated the most from the intended porosity compared to larger unit cell designs. Various studies have found that a reduction in as-built porosity of SLM printed scaffolds is most affected by the smaller unit cell sizes [3], [9]–[11]. Few studies have reported an increase in porosity in some of their as-built gyroid samples [7], [8]. On the other hand, surface area increased as an average of 30% in all samples (Figure 9.b.). This is due to the presence of partly sintered particles attached to the walls as well as the non-smooth walls of the scaffolds (Figure 8.a.). Timercan et al. [3] has also reported an increase in surface area in the gyroids samples printed in Ti-6Al-4V powder by SLM.

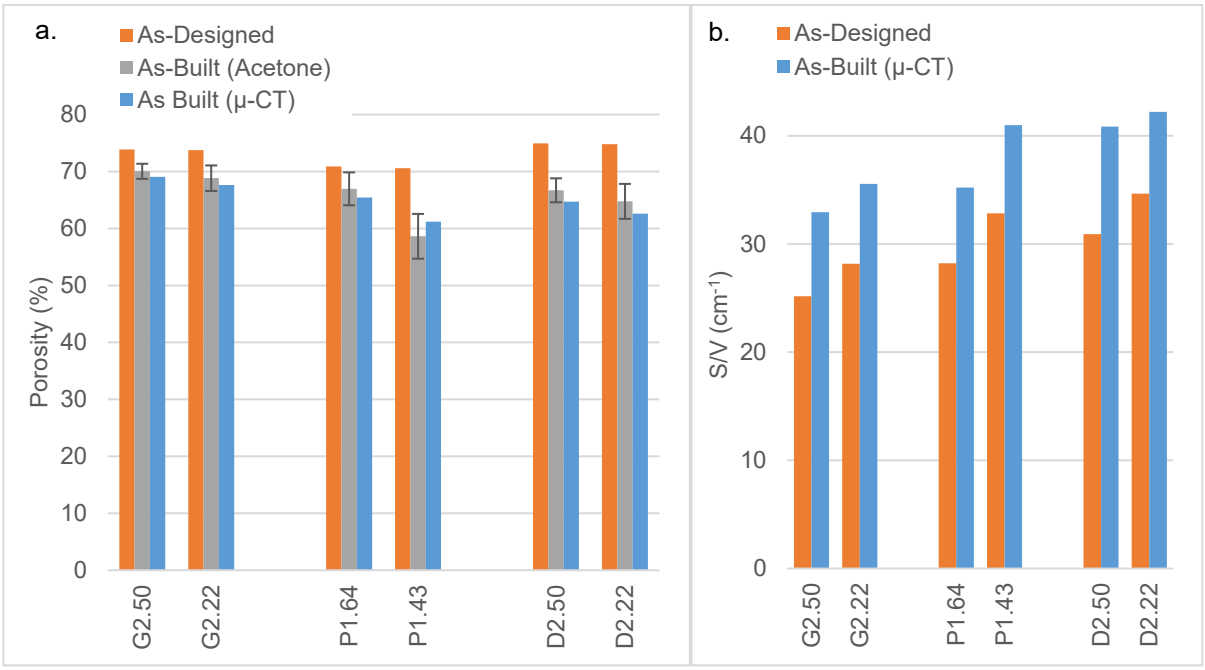

Figure 9. Comparison of as-designed and as-built structure's morphology. a. As-designed vs as-built porosity by acetone method and µ-CT, b. Surface area per unit volume (S/V).

The median and median absolute deviation (MAD) values of sheet thickness and pore size are shown in Figure 10. Gyroid and diamond have smaller variations in intended sheet thickness and pore size compared to the primitive structures. When looking at the values of as-built samples, the sheet thickness of all samples increased while a reduction in median pore diameter was recorded. Similar findings were made by other researchers [3], [9]–[11] for sheet-based gyroids. The most deviation in sheet thickness from intended values were found in the diamond structures. Both gyroids had the highest pore diameters followed by P1.64 and both diamonds while P1.43 had the least pore size among all. However, all pore sizes were larger than the minimum recommended value of 300 µm [2], making them all suitable for bioengineering applications.

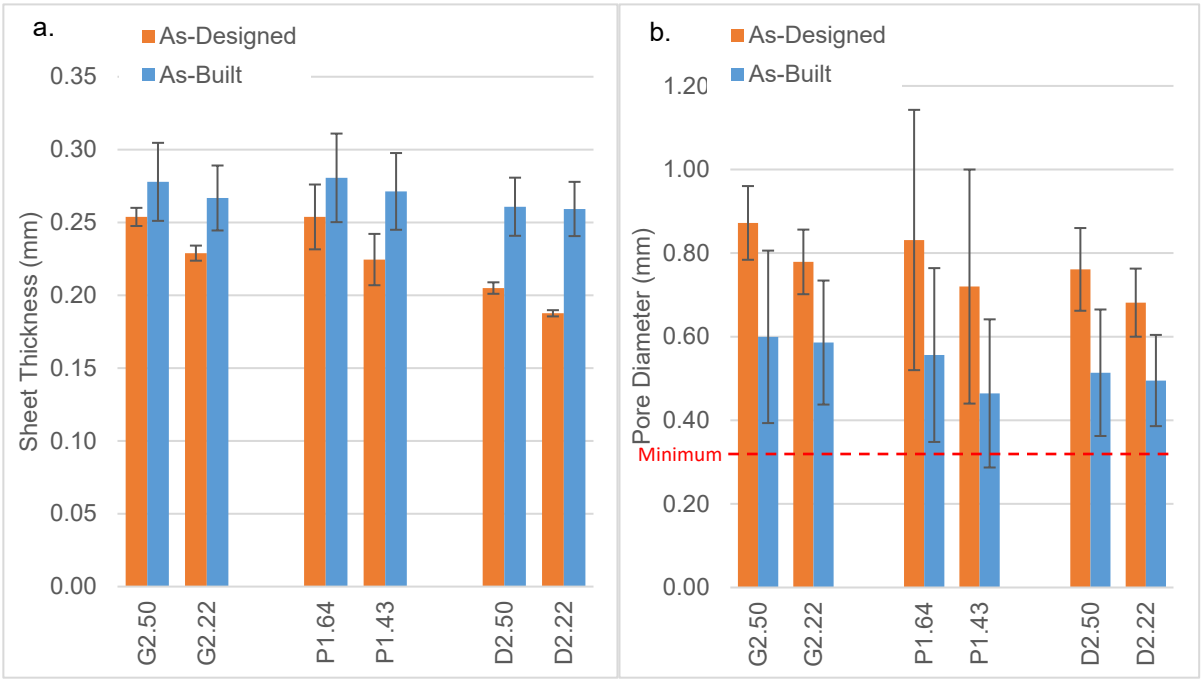

Figure 10. As-designed vs as-built median (± MAD) values for: a. Sheet thickness, b. Pore diameter - minimum pore diameter for bone tissue engineering is shown.

3.4 Compression Testing

Figure 11 compares the effective elastic moduli of as-designed models (by FEA) and as-built scaffolds (by physical testing and image-based meshless simulations). The elastic moduli of as-designed models obtained by FEA was found to be similar for both variants of each scaffold type despite different sheet thickness and pore sizes (Figure 11.a.). This is due to their similar porosity and it is with good agreement with Ashby-Gibson theory of relationship between the relative elastic modulus of a porous structure and its volume fraction [33]. Despite the higher intended porosity, diamond designs exhibited stiffer behaviours with high moduli compared to the gyroids in FEA simulations.

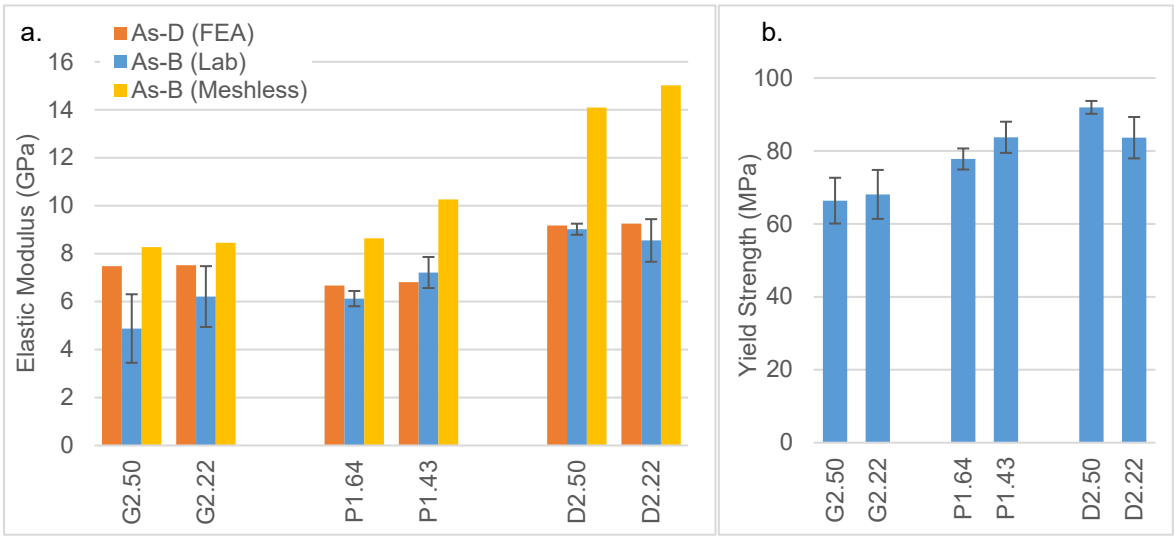

Figure 11. Mechanical properties. a. Effective elastic modulus, as-designed (by FEA) vs as-built (by lab test and meshless methods), b. Yield strength of as-built samples.

The lab test results (Figure 11.a. and b.) show that D2.50 has the highest modulus and yield strength among all variants and G2.50 had the lowest values. The predicted FEA values were very close to the as-built results for both primitive and diamond structures. In case of Gyroids, FEA overestimated the modulus values, as other studies [7], [11] have found. Nonetheless, we found that the as-built elastic modulus of all six scaffolds included in this study lie within the range of trabecular human bone properties (1.5-11.2 GPa), ensuring an effective load transfer between bone and scaffold and avoiding stress-shielding effect [34].

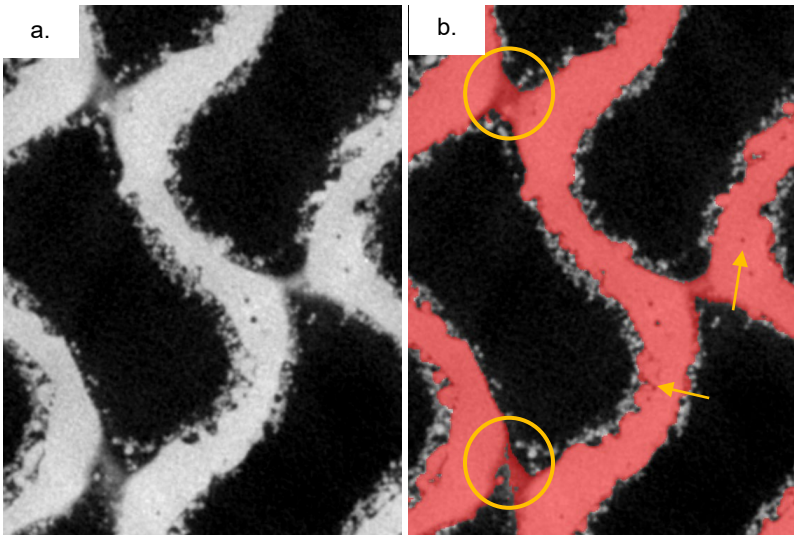

Figure 12.a. CT scan image of G2.25 scaffold. Image thresholding method is limited in capturing details such as closed porosities and fissures in the structure. Arrows show closed porosities were excluded in thresholding; b. Circles highlight the region falsely recognized as solid part of the geometry.

For image-based simulations, the reconstructed digital models of the scaffolds were simulated by a meshless method and the moduli obtained are plotted in Figure 11.a. There is a significant deviation between the lab test and meshless method results for all scaffolds. The simulation results of the as-built diamond scaffolds deviate the most from physical test results. The split model strategy (see Section 3.2.2) was also tested on as-built STL models of D2.22 and P1.43 scaffolds. However, the results were not affected and therefore only the results of unsplit models of 4x4x4 cell configuration are reported in this study.

In an attempt to explain the high stiffness values obtained by this meshless method, the CT scan image with thresholding is shown in Figure 12.b. The image shows the limitation of scan resolution to capture the geometry details of the scaffold. The thresholding method ignored smaller closed porosities at many places and falsely recognized some regions as part of the scaffold envelope. These factors derived in a lower porosity of the digital model compared to lab tested porosity of the samples (Figure 9.a.). These lower porosity models with missing structural details (such as voids and fissures) would lead to a stiffer mechanical response. Another contributing factor might be the limitation of the meshless software to handle the size and complexity of the part geometry as this has been observed in the static analysis of as-designed models in Section 3.2.2.

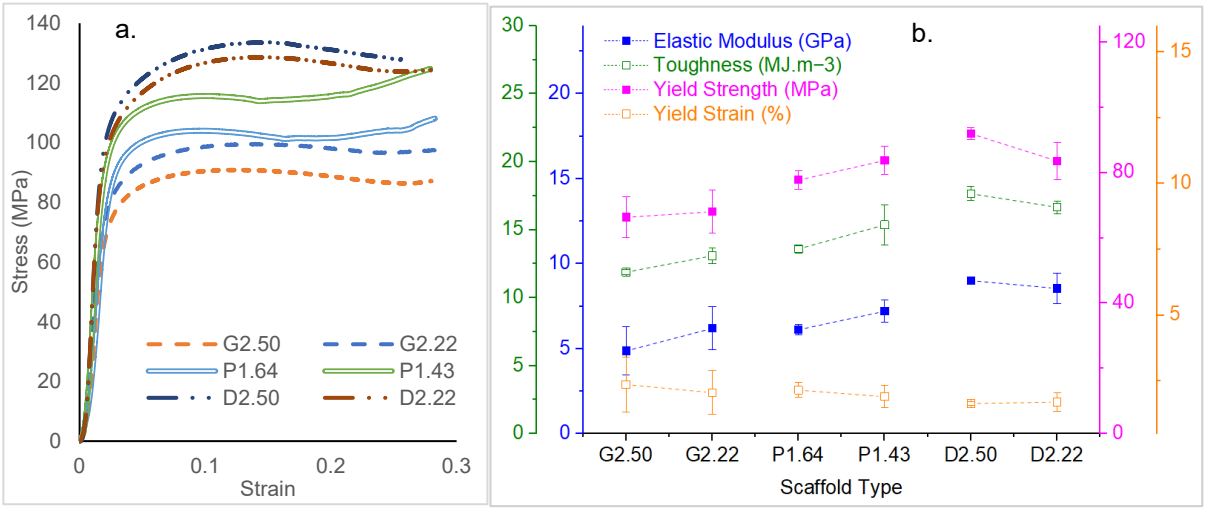

Figure 13. Compression lab testing of as-built samples, a. Stress-strain curves of scaffolds, b. Comparison of elastic modulus, toughness, yield strength and yield strain.

The stress-strain curves of gyroid and diamond structures show similar trends in the plastic region which display a bending-dominant nature. The curve of primitive structures prominently displays plateau stress region due to its stretch-dominant behaviour (Figure 13.a.). Similar influences of lattice topology on compression properties was found by Lu et al. in their study on TPMS structures [35]. The values of elastic modulus, toughness and yield strength were higher, while yield strain values were lower in smaller unit cells compared to their larger counterpart of gyroid and primitive structures (Figure 13.b.). This might be due to larger deviation of as-built porosity from as-designed in variants with smaller unit cells. However, this trend was reversed in the case of diamond structure despite the lower porosity of D2.22 scaffold, which might be explained by the peculiarities of this different topology.

4 Conclusions

In this study we evaluated the manufacturability of sheet-based TPMS structures with intended mechanical and morphological properties suitable for bioengineering applications. The mechanical properties of as-designed structures were evaluated by FEA and results were validated by physical testing of SLM printed scaffolds. Image based meshless simulations were also used to determine the stiffness of as-built models. The findings of the study are summarized as follows:

- The porosity of as-built scaffolds was achieved in the range of 59-70% with surface area 33-42 cm^{-1}. The as-built pore sizes were between 460 to 580 microns. These values lie in the suitable range for bioengineering applications.
- FEA static analysis provides good estimations of intended mechanical properties of scaffolds structures with an average deviation of 11% from lab results. Lab testing of as-built samples

resulted in stiffness range of 5-9 GPa and yield strength of 66-92 MPa. With these mechanical properties, these structures can provide strong support for bone regeneration and osseointegration without causing stress shielding.

- Due to limited accuracy of micro-CT devices, geometric details of porous structures could not be captured precisely. Moreover, the image segmentation and thresholding methods play a critical role in making accurate digital models of scaffolds. We found that meshless methods overestimate the compression properties of the as-built structures. This problem may be addressed by using smaller scaffold models with higher CT resolution to improve the accuracy of the method.

5 Acknowledgement

This research work is supported by a Wolfson School PhD Scholarship and EPSRC (grant number EP/V007335/1).

6 References

[1] M. F. Ashby, “The properties of foams and lattices,” *Philos. Trans. R. Soc. A Math. Phys. Eng. Sci.*, vol. 364, no. 1838, pp. 15–30, 2006, doi: 10.1098/rsta.2005.1678.

[2] C. Torres-Sanchez *et al.*, “Comparison of Selective Laser Melted Commercially Pure Titanium Sheet-Based Triply Periodic Minimal Surfaces and Trabecular-Like Strut-Based Scaffolds for Tissue Engineering,” *Adv. Eng. Mater.*, vol. 24, no. 1, Jan. 2022, doi: 10.1002/adem.202100527.

[3] A. Timercan, V. Sheremetyev, and V. Brailovski, “Mechanical properties and fluid permeability of gyroid and diamond lattice structures for intervertebral devices: functional requirements and comparative analysis,” *Sci. Technol. Adv. Mater.*, vol. 22, no. 1, pp. 285–300, 2021, doi: 10.1080/14686996.2021.1907222.

[4] S. C. Kapfer, S. T. Hyde, K. Mecke, C. H. Arns, and G. E. Schröder-Turk, “Minimal surface scaffold designs for tissue engineering,” *Biomaterials*, vol. 32, no. 29, pp. 6875–6882, 2011, doi: 10.1016/j.biomaterials.2011.06.012.

[5] O. Al-Ketan, R. K. A. Al-Rub, and R. Rowshan, “Mechanical Properties of a New Type of Architected Interpenetrating Phase Composite Materials,” *Adv. Mater. Technol.*, vol. 2, no. 2, pp. 1–7, 2017, doi: 10.1002/admt.201600235.

[6] D. Karaman and H. Ghahramanzadeh Asl, “The effects of sheet and network solid structures of similar TPMS scaffold architectures on permeability, wall shear stress, and velocity: A CFD analysis,” *Med. Eng. Phys.*, vol. 118, no. February, p. 104024, 2023, doi: 10.1016/j.medengphy.2023.104024.

[7] A. Timercan, P. Terriault, and V. Brailovski, “Axial tension/compression and torsional loading of diamond and gyroid lattice structures for biomedical implants: Simulation and experiment,” *Mater. Des.*, vol. 225, p. 111585, 2023, doi: 10.1016/j.matdes.2022.111585.

[8] F. S. L. Bobbert *et al.*, “Additively manufactured metallic porous biomaterials based on minimal surfaces: A unique combination of topological, mechanical, and mass transport properties,” *Acta Biomater.*, vol. 53, pp. 572–584, Apr. 2017, doi: 10.1016/j.actbio.2017.02.024.

[9] M. Ebrahimi, A. Kermanpur, and M. Kharaziha, “The effects of pore size and heat treatment on compression and corrosion behaviors of Ti-6Al-4V sheet-based gyroid implants fabricated by laser powder-bed fusion process,” *J. Mater. Res. Technol.*, vol. 26, pp. 7707–7721, 2023, doi: 10.1016/j.jmrt.2023.09.130.

[10] S. A. Naghavi *et al.*, “Mechanical Characterisation and Numerical Modelling of TPMS-Based Gyroid and Diamond Ti6Al4V Scaffolds for Bone Implants: An Integrated Approach for Translational Consideration,” *Bioengineering*, vol. 9, no. 10, p. 504, 2022, doi: 10.3390/bioengineering9100504.

[11] S. Ma *et al.*, “Manufacturability, Mechanical Properties, Mass-Transport Properties and Biocompatibility of Triply Periodic Minimal Surface (TPMS) Porous Scaffolds Fabricated by Selective Laser Melting,” *Mater. Des.*, vol. 195, 2020, doi: 10.1016/j.matdes.2020.109034.

[12] L. C. Zhang, D. Klemm, J. Eckert, Y. L. Hao, and T. B. Sercombe, “Manufacture by selective laser melting and mechanical behavior of a biomedical Ti-24Nb-4Zr-8Sn alloy,” *Scr. Mater.*, vol. 65, no. 1, pp. 21–24, 2011, doi: 10.1016/j.scriptamat.2011.03.024.

[13] S. Ghouse, “Optimizing additive manufactured porous structures for orthopaedics,” Imperial College London, 2019. doi: https://doi.org/10.25560/78640.

[14] C. Yan, L. Hao, A. Hussein, P. Young, and D. Raymont, “Advanced lightweight 316L stainless steel cellular lattice structures fabricated via selective laser melting,” *Mater. Des.*, vol. 55, pp. 533–541, 2014, doi: 10.1016/j.matdes.2013.10.027.

[15] C. Peng and P. Tran, “Bioinspired functionally graded gyroid sandwich panel subjected to impulsive loadings,” *Compos. Part B Eng.*, vol. 188, no. July 2019, p. 107773, 2020, doi: 10.1016/j.compositesb.2020.107773.

[16] L. Emanuelli *et al.*, “Manufacturability of functionally graded porous β-Ti21S auxetic architected biomaterials produced by laser powder bed fusion: comparison between 2D and 3D metrological characterization,” *Int. J. Bioprinting*, vol. X, no. 3D Printing of Advanced Biomedical Devices, 2023.

[17] U. Simsek, A. Akbulut, C. E. Gayir, C. Basaran, and P. Sendur, “Modal characterization of additively manufactured TPMS structures: comparison between different modeling methods,” *Int. J. Adv. Manuf. Technol.*, vol. 115, no. 3, pp. 657–674, 2021, doi: 10.1007/s00170-020-06174-0.

[18] L. M. Evans, E. Sözümert, B. E. Keenan, C. E. Wood, and A. du Plessis, *A Review of Image-Based Simulation Applications in High-Value Manufacturing*, vol. 30, no. 3. Springer Netherlands, 2023. doi: 10.1007/s11831-022-09836-2.

[19] M. Doroszko and A. Seweryn, “Numerical modeling of the tensile deformation process of sintered 316L based on microtomography of porous mesostructures,” *Mater. Des.*, vol. 88, pp. 493–504, 2015, doi: 10.1016/j.matdes.2015.09.006.

[20] M. Doroszko and A. Seweryn, “A new numerical modelling method for deformation behaviour of metallic porous materials using X-ray computed microtomography,” *Mater. Sci. Eng. A*, vol. 689, no. November 2016, pp. 142–156, 2017, doi: 10.1016/j.msea.2017.02.055.

[21] D. Mahmoud and M. A. Elbestawi, “Selective laser melting of porosity graded lattice structures for bone implants,” *Int. J. Adv. Manuf. Technol.*, vol. 100, no. 9–12, pp. 2915–2927, 2019, doi: 10.1007/s00170-018-2886-9.

[22] Standard Test Methods of Compression Testing of Metallic Materials at Room Temperature, ASTM E9-19, ASTM International. 2019. doi: 10.1520/E0009-19.

[23] Standard Test Method for Determination of Carbon in Refractory and Reactive Metals and Their Alloys by Combustion Analysis, ASTM E1941-10, ASTM International. 2016. doi: 10.1520/E1941-10R16.

[24] Standard Test Method for Determination of Oxygen and Nitrogen in Titanium and Titanium Alloys by Inert Gas Fusion, ASTM E1409-13, ASTM International. 2013. doi: 10.1520/E1409-13.

[25] Standard Test Method for Determination of Hydrogen in Titanium and Titanium Alloys by the Inert Gas Fusion Thermal Conductivity/Infrared Detection Method, ASTM E1447-09, ASTM International. 2009. doi: 10.1520/E1447-09.

[26] Standard Test Method for Analysis of Titanium and Titanium Alloys by Direct Current Plasma and Inductively Coupled Plasma Atomic Emission Spectrometry (Performance-Based Test Methodology), ASTM E2371-13, ASTM International. 2013. doi: 10.1520/E2371-13.

[27] A. Fedorov *et al.*, “3D Slicer as an image computing platform for the Quantitative Imaging Network,” *Magn. Reson. Imaging*, vol. 30, no. 9, pp. 1323–1341, 2012, doi: 10.1016/j.mri.2012.05.001.

[28] T. Hildebrand and P. Rüegsegger, “A new method for the model-independent assessment of thickness in three-dimensional images,” *J. Microsc.*, vol. 185, no. 1, pp. 67–75, 1997, doi: 10.1046/j.1365-2818.1997.1340694.x.

[29] L. Emanuelli *et al.*, “Metrological characterization of porosity graded β-Ti21S triply periodic minimal surface cellular structure manufactured by laser powder bed fusion,” *Int. J. Bioprinting*, vol. 9, no. 4, 2023, doi: 10.18063/ijb.729.

[30] I. Maskery, A. O. Aremu, L. Parry, R. D. Wildman, C. J. Tuck, and I. A. Ashcroft, “Effective design and simulation of surface-based lattice structures featuring volume fraction and cell type grading,” *Mater. Des.*, vol. 155, pp. 220–232, 2018, doi: 10.1016/j.matdes.2018.05.058.

[31] J. P. Kruth, P. Mercelis, J. Van Vaerenbergh, L. Froyen, and M. Rombouts, “Binding mechanisms in selective laser sintering and selective laser melting,” *Rapid Prototyp. J.*, vol. 11, no. 1, pp. 26–36, 2005, doi: 10.1108/13552540510573365.

[32] C. Torres-Sanchez, J. Wang, K. Kottut, B. Moore, and P. P. Conway, “Electrochemical removal of secondary roughness on selective laser melted titanium with an ethylene–glycol-based electrolyte,” *Mater. Lett.*, vol. 343, no. April, p. 134367, 2023, doi: 10.1016/j.matlet.2023.134367.

[33] L. J. Gibson and M. F. Ashby, *Cellular Solids: Structure and Properties*, 2nd ed. Cambridge University Press, 1997.

[34] C. Torres-Sanchez, F. R. A. Al Mushref, M. Norrito, K. Yendall, Y. Liu, and P. P. Conway, “The effect of pore size and porosity on mechanical properties and biological response of porous titanium scaffolds,” *Mater. Sci. Eng. C*, vol. 77, pp. 219–228, 2017, doi: 10.1016/j.msec.2017.03.249.

[35] Y. Lu, L. L. Cheng, Z. Yang, J. Li, and H. Zhu, “Relationship between the morphological, mechanical and permeability properties of porous bone scaffolds and the underlying microstructure,” *PLoS One*, vol. 15, no. 9 September, pp. 1–19, 2020, doi: 10.1371/journal.pone.0238471.